



Production and Characterization of an Economical 1100 MPa Advanced High-Strength Silicon-Containing Steel

Hossam Halfa¹ · Amer Eid Amer² · Mamdouh Eissa¹

Received: 25 August 2023 / Revised: 11 November 2023 / Accepted: 19 November 2023 / Published online: 10 January 2024
© The Author(s) 2024

Abstract

In this investigation, an attempt has been made to identify the metallurgical properties with the change of silicon contents, either theoretically by utilizing Thermo-Calc (the Scheil–Gulliver model implemented in the Thermo-Calc software) or JMatPro software, as a computational prediction technique, in addition to experimental examinations by dilatometer. Microstructures of investigated steels were evaluated optically at low magnification using optical microscopy. Scanning electron microscopy was used to study the observed microstructure at high magnification. ASTM standard specification E-8 was utilized for measuring the tensile property values, while fracture surfaces of the tensile samples were inspected by EDS (point-analyzer) employed in scanning electron microscopy. The investigated steel's as-polished surface was studied using the experimental results, which revealed that the steel microstructure ranged from full-bainitic to full-pearlitic structures according to the variation of silicon contents. The count of non-metallic inclusions decreased and vice versa by the area occupied by non-metallic inclusions with the rising silicon content. The steel containing silicon of 0.87 wt.% has the best toughness combined with high tensile strength and hardness incomparable with conventional steel. Elongation (16.2%) combined with an ultimate tensile strength (1113 MPa) was achieved for the steel containing 0.87 wt.% Si.

Keywords High strength · Phase transformation · Thermo-Calc · JMatPro · Mechanical

Introduction

Currently, the essential goal of steel manufacturers and technologists in the metallurgical industry is to transport steel with sophisticated performance and properties, extraordinary weight-to-strength ratios, and truncated expenses to the market.

Advanced high-strength steels (AHSSs) were recommended for utilization to perform the mentioned purposes; on the contrary, titanium alloys, aluminum alloys, and high-alloyed steels are not favored because of the elevated price of manufacturing crude material. Remarkable attention is devoted to multiphase steel studies because of their impressive mechanical characteristics. TRIP steels (transformation

induced plasticity steels) are famous advanced high-strength steels (second generation) members. While ferritic-bainitic steel, bainitic steel, silicon-containing austempered steels, and carbide-free bainitic steel are respected as third-generation steel, it is attractive to investigate its development [1–4]. Since discovering bainitic steel with high strength and good toughness, ultrafine bainitic nanostructured steel has been widely applied in most engineering parts. A recent process for manufacturing the bainitic steel is subjected to a discontinuous cooling program, which entails fast-tracked cooling at a rate of 1 to 10 °C/s from the austenite phase region to a stop cooling temperature range of 500 to 300 °C, then cooled further to an ambient atmosphere temperature. The bainitic steel from which produced steel is not carbide-free [5–10].

Metallurgists designing and producing advanced steel defined carbide-free bainite (CFB) as the bainitic microstructure acquired without carbide precipitation during the austempering of the steels [11–15]. Because of the combination of superior technological possessions (excellent wear resistance, high tensile properties, good weldability, and enhancing corrosion properties) with the truncated production cost, carbide-free bainite (CFB) steels are counted as a

✉ Hossam Halfa
dr.hossam@cmrdi.sci.eg; hossamhalfa@gmail.com

¹ Steel Technology Department, Central Metallurgical R&D Institute (CMRDI), Helwan, Egypt

² Mechanical Design and Production Engineering Dept., Faculty of Engineering, Beni-Suef University, Beni Suef 62511, Egypt

promising class of HSS (high-strength steels) [11–15]. Carbide-free bainitic (CFB) steels are in development because of their excellent technological properties, which are demanded in different appliances, e.g., building construction, marine concrete, and highway (rails track).

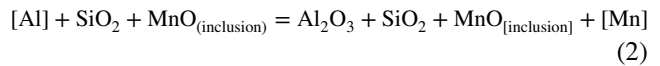
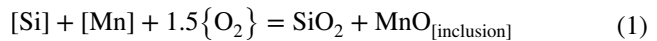
Additive silicon with more than 1 wt.% inhibits cementite formation [16–20]. In addition, silicon promotes carbon enrichment of austenite during austempering [21] and allows its preservation at ambient atmosphere temperature. The research published by Zhu et al. [22] highlighted that silicon hinders static and dynamic recrystallization. Also, silicon diminishes the grain evolution of retained austenite and improves its constancy right to ambient temperature. In traffic research work, Matsumura et al. [23] established that silicon decelerates down bainitic kinetic transformation and enlarges its field stability. Furthermore, increased silicon with considerable contents increases the critical transformation temperatures (Ac1 and Ac3) in the iron-cementite (Fe-Fe₃C) equilibrium phase diagram [19].

Many studies investigated the deoxidation of steel by silicon and manganese before casting [24–27]. They observed that Si-Mn deoxidation has an advantage over aluminum deoxidation in that the principal inclusions are usually liquid [25]. MnO, SiO₂, and Al₂O₃ complicated non-metallic inclusions were predicted during Si-Mn killed steels, with Al₂O₃ originating from ferroalloys and refractories [26]. The inclusion population is classified into three primary groups: “oxides,” “mixed,” and “sulfides,” with sulfur serving as a differentiating factor.

The largest-size inclusions in silicon and manganese-killed steel, according to Thapliyal et al. [24], were MnO-SiO₂-based inclusions with some Al₂O₃. MnS was the dominant phase in sulfur-rich inclusions or the dominant phase in oxide inclusions. MnS precipitated on existing oxide inclusions in mixed inclusions, whereas sulfide inclusions formed owing to sulfur segregation after solidification. As a result, mixed inclusions had bigger average inclusion sizes than sulfide inclusions. At around 1400 °C, MnS precipitation begins in steel during cooling. In contrast, heterogeneous MnS nucleation on preexisting oxide inclusions was observed.

Lyu et al. [27], on the other hand, released a detailed paper titled “Understanding the Formation and Evolution of Oxide Inclusions in Si-Deoxidized Spring Steel.” According to Lyu et al., manganese and silicon are specifically oxidized by ambient oxygen due to the examined spring steel’s high silicon and manganese content. Furthermore, their products raise non-metallic inclusions, which are usually one or two sizes larger than deoxidation inclusions; because of equation (1), oxygen was captured from the environment and quickly reacted with the dissolved [Si] and [Mn], forming large amounts of SiO₂-MnO inclusions particles in the liquid steel. As

shown in Eq (2), the dissolved [Al] in the molten steel interacted with the produced SiO₂-MnO inclusions to generate Al₂O₃-SiO₂-MnO inclusions.



Many researchers stated that the technological properties of studied steels were notably influenced by the presence, size distribution, amount, and shape of non-metallic inclusions [28–34]. The mentioned reviews revealed that the source of non-metallic inclusions in steel production is classified into endogenous and exogenous non-metallic inclusions [28–34]. The size and shape factor of NMI (non-metallic inclusions) and their impact on the technological properties were controlled by knowing their origin. For example, hard oxide particles have the most harmful influence on the overall technological properties, especially the mechanical properties of steel. The oversized non-metallic inclusion particles may be catastrophic, whereas the minute sizes NMI are usually not harmful and inevitable.

The literature recognized that the volume fraction of NMI remaining in liquid steels and end steel products was significantly reduced by utilizing NMI removal techniques [35–37] and new secondary refining and remelting technologies [38–40] in steel production processes. The NMI in clean steels consists of a cluster of minute-size NMI particles and a few oversize NMI particles. The size and size distribution addition to the threshold size of the inclusion in a presented volume of liquid steel is critical for the technological properties of produced steel. The few oversize inclusions affected the clean steel mechanical properties. The expectation of steel mechanical properties is decided by theoretical models involving the threshold of inclusion diameter [41]. There are many principal effects on the crack initiation of NMI, such as chemistry, size, morphology, and location relative to the surface density [42]. Brittle oxide inclusions are more harmful to mechanical properties than sulfide inclusions in the steels and have a high deformability index.

The investigation by Murakami et al. [36, 37] remarked that an intermediate position behavior was kept for siliceous inclusions. Large exogenous inclusions (refractory or slag particles) are eternally damaging to the technological characteristic of steel due to their outside and shape irregularities. Many investigators [43, 44] show that residual tensile stresses generated around the non-metallic inclusions approach the steel matrix yield strength during cooling due to the low NMI thermal expansion coefficient. Therefore, NMI size-controlled the circumferential stress

field intensified and concentrated close to non-metallic inclusions. The mechanical properties reasonably decided the suitability of steels for their technological application, so for inclusion evaluation, the fracture tests were beneficial methods.

The central purpose of this contribution is to produce and develop steel with a moderate strength of nearly 1100MPa, with total elongation > 10%. Furthermore, another research task is to identify the metallurgical evolution with the variation of silicon contents.

Experimental Work

Chemical Composition Designing

Silicon steel alloys containing more than the standard low-alloyed medium-carbon steel were developed by raising the silicon content to 3 wt.% to produce new and advanced carbide-free bainitic steel. More chromium was mixed in the studied steel to improve the hardness of the material. Table 1 represents an experimental steel set of chemical compositions.

Production Technique

The steel ingots studied were manufactured by smelting basic materials in a hundred kgs capacity open-air induction melting furnace performed in medium frequency. The crude material chemical compositions in weight percent utilized for producing the studied steel, as shown in Table 2. Molten steels were deoxidized preliminarily to enhance the absorptivity of alloying elements. The deoxidizing preliminary was performed using aluminum and ferrosilicon magnesium. Moreover, to eliminate or diminish the internal defects in the

Table 1 Investigated steel's chemical composition

Chemical composition, wt.%					
C	Si	Mn	Cr	Ni	Fe
0.35–0.45	0.2–3.0	<0.5	=1	=1	Balance

Table 2 Chemical composition of raw materials utilized for producing investigated steel alloys

Charged material	Chemical composition wt.%									
	C	Mn	S	P	Si	Ni	Ti	Cr	Al	Fe
Steel scrap	0.52	0.37	0.012	0.013	1.52	0.32	0.003	0.03	–	Balance
Ni-metal	–	–	–	–	–	99.6	–	0.3	–	–
Aluminum	–	–	–	–	0.3	–	–	–	99.7	–
Ferrosilicon	7.93	–	0.003	0.025	1.98	–	–	73	–	Balance
Ferromanganese	6.5	73.1	0.03	0.35	1.32	–	–	–	–	Balance
Ferrosilicon	0.01	0.35	0.01	0.035	75	–	–	0.25	1.95	Balance

casting steel, argon gas was blown into melt before tapping into a steel mold. The argon injection is not only to decrease the dissolved gases but also to increase the homogeneity of the steel melt and increase the chance of non-metallic inclusion floating up. NMI captured by slag film above the melt and modified by additive calcium silicon ($\text{Ca}_{30}\text{Si}_{60}$) alloy. The slag was skimmed just before pouring the molten metal. The melt was poured from the furnace crucible into preheated steel chill molds at 800 °C after adjusting the melt temperature to about 1550 °C.

Thermo-Calc Investigation (Non-equilibrium Condition)

The microstructure of the investigating steel can be easily predicted and established on thermodynamical estimation and the actual chemical composition, in addition to the amount in volume fraction % and chemical composition of each phase. The microstructure evolution as a variation of silicon contents is theoretically estimated employing the Scheil–Gulliver model executed in the Thermo-Calc program. Non-equilibrium thermodynamical data were calculated for the studied steel composition belonging to the several elements Fe–Si–Ni–Mn–Cr–C system. Table 3

Table 3 Models of the constituents respected in the Scheil–Gulliver simulations

Phase	Numbers of sub-lattice	Numbers of sites per sub-lattice	Sub-lattice species (Va = Vacancy)
Liquid	1	1	C, Cr, Fe, Si, Mn, Ni
FCC (γ -austenite)	2	1:1	Cr, Fe, Mn, Ni, C, Va
BCC (α -ferrite)	2	1:3	Cr, Fe, Si, Va
FCC_A2#2 (MC)	2	1:1	Mo, V, W:C
M_3C (cementite)	2	3:1	Cr, Fe, Mo, V, W:C
M_7C_3	2	7:3	Cr, Fe: C
M_{23}C_6	3	20:3:6	Cr, Fe, W:C

shows the constituents in the database were categorized corresponding to a sub-lattice model [45–47].

Dilation Test

LINSEIS TA Evaluation V2.3 dilatometer was utilized to understand the different phases with temperature changes of actual steel specimens during heating dilation tests. Steel specimens (with 20mm height*4mm diameter dimensions) were sliced utilizing a wire cutting machine with the more extended dimension parallel to the longitudinal side and used to determine transformation temperatures (Ac1 and Ac3), austenitizing temperatures, and homogenization temperature, in addition to hot forging temperature.

The sample temperature was regulated and observed utilizing a type S thermocouple. During the heating and isothermal segments, argon pressure of approximately 1×10^{-4} m bar was induced in the sample chamber.

The dilation plots were evaluated to expect the microstructural phase transformation behavior. After completing the dilation test, the samples of microstructural observation were taken from the studied steel samples at the midsection. These specimens were affixed in an epoxy resin, polished per standard metallography procedures, and etched using a 2% Nital solution. Furthermore, the steel specimens were tested optically by Leco microscopes at different magnifications. The hardness test was realized using a universal hardness testing machine and averaged the ten readings.

The constituent's volume fraction of the studied steel specimens was computed from the optical microstructure photographs by adopting an image analysis procedure utilizing Image J software.

Forging

The forging process is a plastic deformation process characterized by its ability to eliminate internal voids/gas pockets that weaken the investigated steel specimens. Besides, it delivers enhanced chemical homogeneity, guarantees appropriate grain flow orientation, and intensified structural strength. Forging operation was achieved utilizing a pneumatic press with a one-ton capacity. The investigated steel specimen was preheated continuously at 15 °C/min until hot forging (homogenized-austenitizing) temperature was attained, predicted by JmatPro software, and measured experimentally by dilation test. Soaking time is determined according to the ingot's sizes. It is worth declaring that the forging process finishes at around 950 °C. The start cylindrical shaped ingots with 100 mm diameter and 250 mm height were forged to produce a rod with a 40 mm diameter. The forging operation has an average strain of 525%, a strain rate of 8.75 s^{-1} and an average speed of 0.262 kg/s. The reheating and forging schedule

assured the elimination of any hot tearing or cracking during the deformation of the steel, even to a small diameter.

Heat Treatment

The JmatPro software was employed to predict different heat treatment parameters of the studied steel specimens. The heat treatment parameters obtained include transformation and homogenization temperatures, austenitization temperatures, and time. On the other hand, the mentioned heat treatment parameters were experimentally determined utilizing a dilatometer test. After the forging operation, the forged samples were normalized by heated linearly at 300 °C/h to homogenized (1000 °C) temperature, held for 10 min, and left to cool freely in the air, as represented by Figure 1. After normalization, forged and normalized samples were heat-treated following a restricted heating cycle. Figure 1 reveals that the heating rate ranged from 300 to 1200 °C/h from room temperature to austenitizing temperature, followed by interrupted cooling. The interrupted cooling process includes cooling from solid solution annealing (austenitizing) temperature to bainitic transformation temperature with a cooling rate less than the critical cooling rate, held for a certain period, and leaving to cool freely in the air.

Mechanical Testing

The technological properties cleared after the heat treatment cycle. The specimen was prepared to standard V-notch Charpy dimension, which measured 10 mm × 10 mm × 55 mm. Impact toughness testing was conducted at an ambient temperature according to ASTM standard specification E23, and a mean of three test results was recorded as the impact toughness value. The forged heat-treated samples were exposed to a unidirectional tensile loading test, and samples were prepared and tested under the ASTM standard specification E-8 requirement. The tensile properties were measured at a strain rate of 0.1 s^{-1} . The results recorded in this study are the average measurement results of three trials.

Results and Discussion

The investigated steel is analyzed for chemical composition after descaling and removing rust from the cast surface. Table 4 tabulates the chemical compositions of the steels under study. It shows that the producing steel chemical composition verified the planned requirement of the study.

Fig. 1 The suggested heat treatment cycles of forged steel

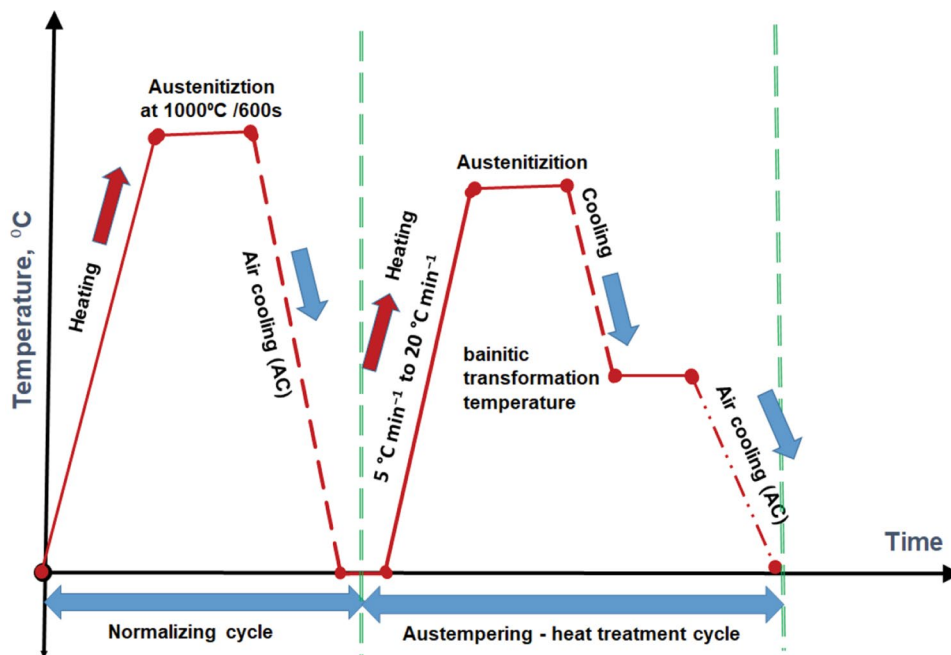


Table 4 Chemical composition wt.% of investigated steels

Steel sample no.	Chemical composition, wt.%					
	C	Si	Mn	Cr	Ni	Fe
AM1	0.39	0.27	0.45	1.06	0.95	Balance
AM2	0.42	0.85	0.38	1.00	0.98	Balance
AM3	0.40	1.60	0.44	1.08	0.96	Balance
AM4	0.37	2.97	0.49	1.03	0.98	Balance

Thermodynamical Evaluation

Figure 2 displays the Schiel–Gulliver diagram (non-equilibrium solidification path diagram) of considered silicon-containing steels. Data obtained from Fig. 2 are extracted and summarized in Table 5.

Notably, the data obtained from Thermo-Calc prediction in non-equilibrium cases are noteworthy. Figure 2 and Table 5 show that increasing the silicon contents of investigating steels diminished the solidus and liquidus temperatures.

The silicon additive to investigating steel encourages the transformation of liquid metal to α -ferrite (BCC) because silicon is a ferritic-stabilizing element. The solidification isopleth reveals that carbon has a higher phase formation effect incomparable with the silicon effect, which may be described as carbon diminishing the BCC-phase area at high temperatures and forcing nucleation of the austenite phase first from the molten steel.

On the other hand, additive silicon to such steel encourages carbide precipitation. Silicon additives significantly affect different constituents' starting formation temperature

and volume fraction percent (amount). Solubility of the alloying element reduces with declining the molten metal temperature, resulting in carbide precipitation, which increases with increased silicon contents. The final expected microstructure of investigating steels included ferrite and carbides. Different volume fraction percent of investigated steel phases and silicon invariants are collected and presented in Table 6.

Non-metallic Inclusions (NMI) Investigation

The discovery of NMI foundations and chemical composition determination is routine in evaluation today. The characteristics of NMI and their impacts on the technological behavior of steels have been well documented. Consequently, the essential claim here concentrated on qualitative considerations, like the size, volume fraction, and distribution of NMI.

Figure 3 exhibits the photograph of NMI presented in investigated steels. Table 7 represents the NMI data obtained utilizing Image J software from as-polished specimen surfaces of investigated steel with a tested area of 25022.2

Fig. 2 Schiel–Gulliver diagram of investigated steel

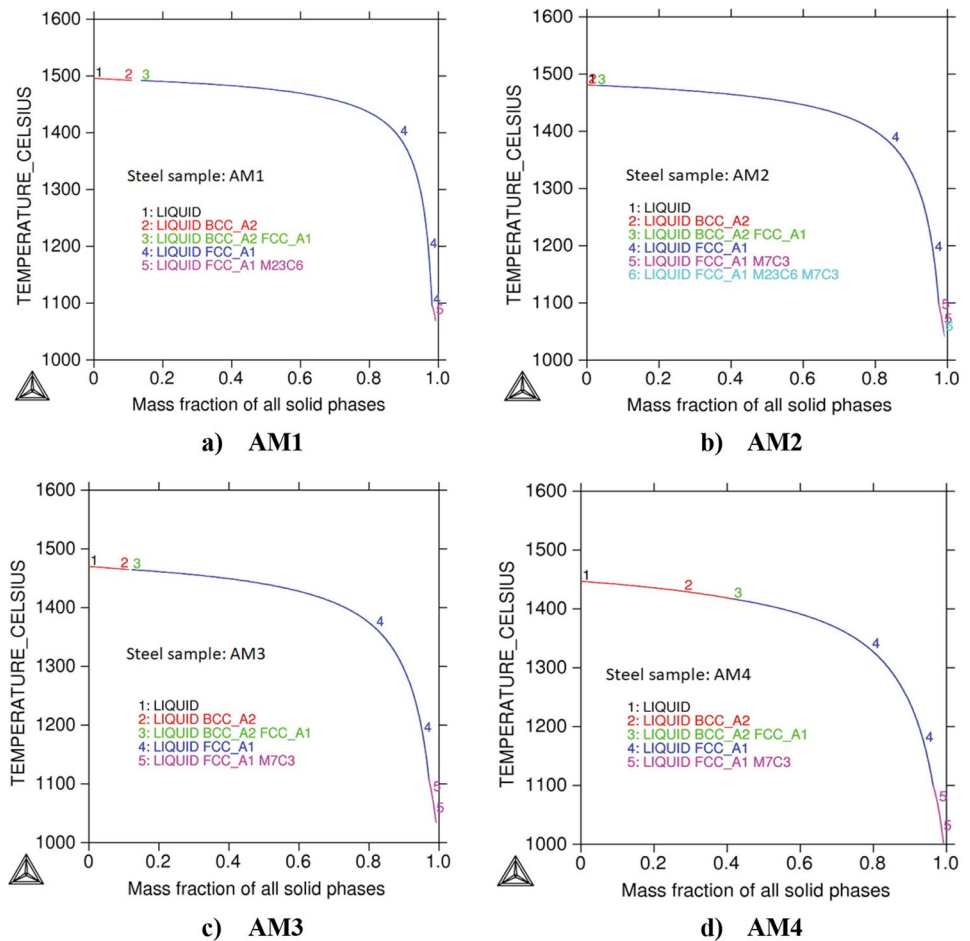


Table 5 The phases' starting temperature of studied steel solidified under non-equilibrium solidification conditions from the molten temperature

Sample No.	Liquidus	BCC	FCC	M ₂₃ C ₆	M ₇ C ₃	Solidus
AM1	< 1498	1498	1492	1098	–	1070
AM2	< 1482	1482	1480	1056	1102	1040
AM3	< 1472	1472	1466	–	1106	1037
AM4	< 1446	1446	1416	–	1099	1005

Table 6 Amount (volume fraction %) of phases after complete solidification based on Thermo-Calc calculation

Steel sample no.	Different phases volume fraction %			
	Ferrite	Carbides		
		Total	M ₂₃ C ₇	M ₇ C ₃
AM1	91.5	8.50	8.50	–
AM2	92.02	7.98	4.30	2.65
AM3	95.55	4.45	–	4.45
AM4	95.96	4.04	–	4.04

μm². The results generally show that non-metallic (NMI) content is shallow, with a small average size. Furthermore, NMI count, the total area of NMI, average size, NMI area,

and circularity increase with the increasing silicon content. Table 7 and Fig. 4 show that although increasing the total area and area fraction %, the average size of NMI for investigated steel remains around 5 μm.

On the other hand, the count and the average size of NMI have a peak for steel containing 0.86% silicon. These peaks may be attributed to several complicated conditions. It is well-known that Al₂O₃ presence in investigated steel may be due to the steel deoxidized by aluminum, ferrosilicon, and ferromanganese, which Al₂O₃ may contaminate. So, the presence of alumina is essentially in aluminum-killed steel or deoxidized by ferrosilicon and ferromanganese.

Figure 5 represents the non-metallic inclusions distribution of investigated steel. However, the mentioned figure emphasizes that the produced steel is clean because the

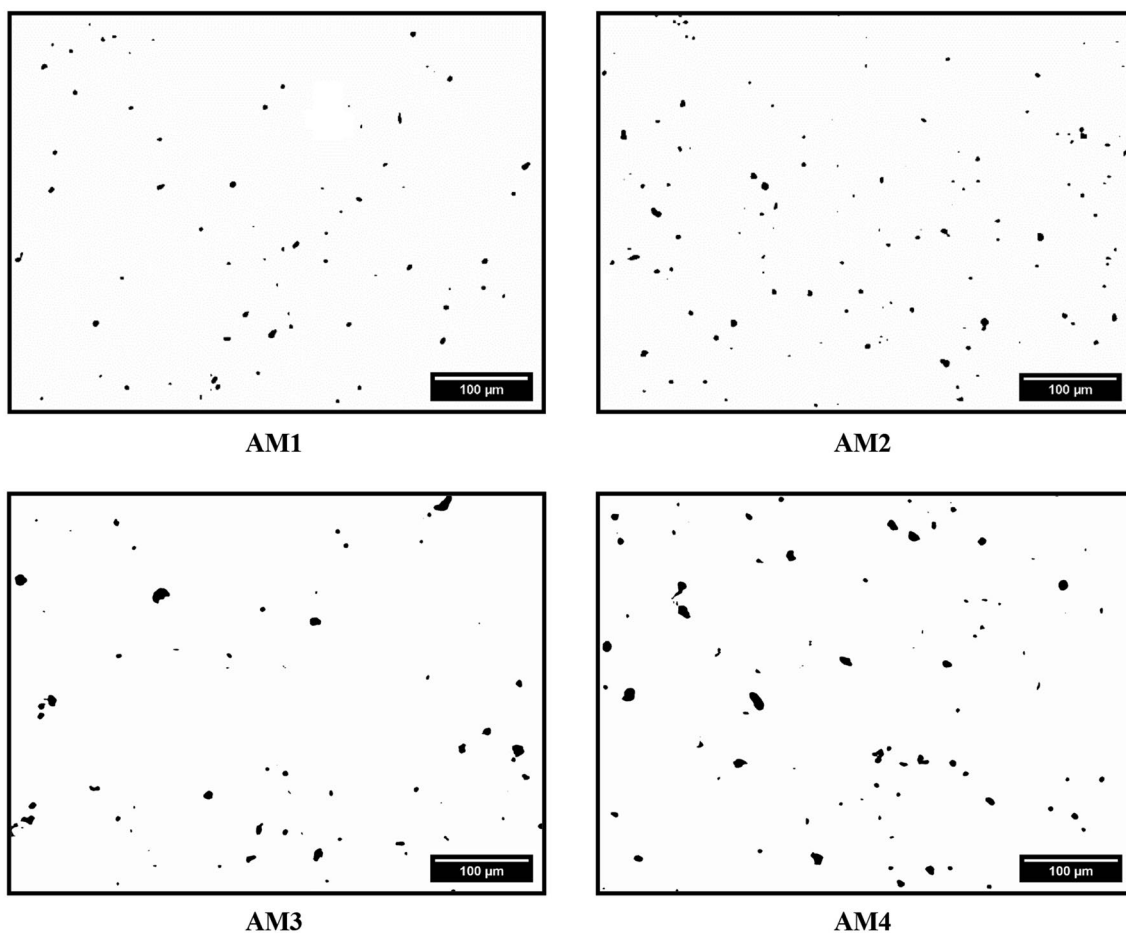


Fig. 3 Photograph of NMI appeared in examined steels

Table 7 The NMI data obtained utilizing Image J software from as-polished specimen surfaces of investigated steel

Steel no.	Si, wt.%	Count	Total area, μm^2	% Area	Average area, μm^2	Average size, μm	Circ.
AM1	0.25	57	1147.6	0.45	19.3	4.96	0.805
AM2	0.87	146	2424	1	16.8	4.63	0.812
AM3	1.59	59	1682.5	0.7	33	6.48	0.8284
AM4	3	80	2745	1.13	35	6.68	0.785

most significant size of NMI is not more than 10 μm . On the other hand, increased silicon content leads to precipitate and agglomerate of the non-metallic inclusion with grain size more considerable than 10 μm . In such steel, alumina works as a nuclei site for non-metallic inclusions. This non-metallic inclusion collects the other deoxidation products, e.g., SiO_2 and MnO ; therefore, complex non-metallic inclusions are made. The size of this inclusion increases with heat time due to the accumulation of deoxidant products. Heat time mainly depends on the melting point of add-alloying elements and their amount.

On the other hand, the shape of the NMI is distinguished by its formation temperature and chemical composition. NMI is exposed to buoyancy force after the formation and coalescences of non-metallic inclusions, which helps it float. The essential purpose of argon blowing is to help non-metallic inclusion float up and be collected in the slag phase or captured by the furnace wall. Large-size non-metallic inclusion can be gotten rid of (removed) from molten steel thanks to argon blowing. Therefore, the remaining non-metallic inclusion has a small and medium size. That is the cause of the decrease in the count and the average size of NMI

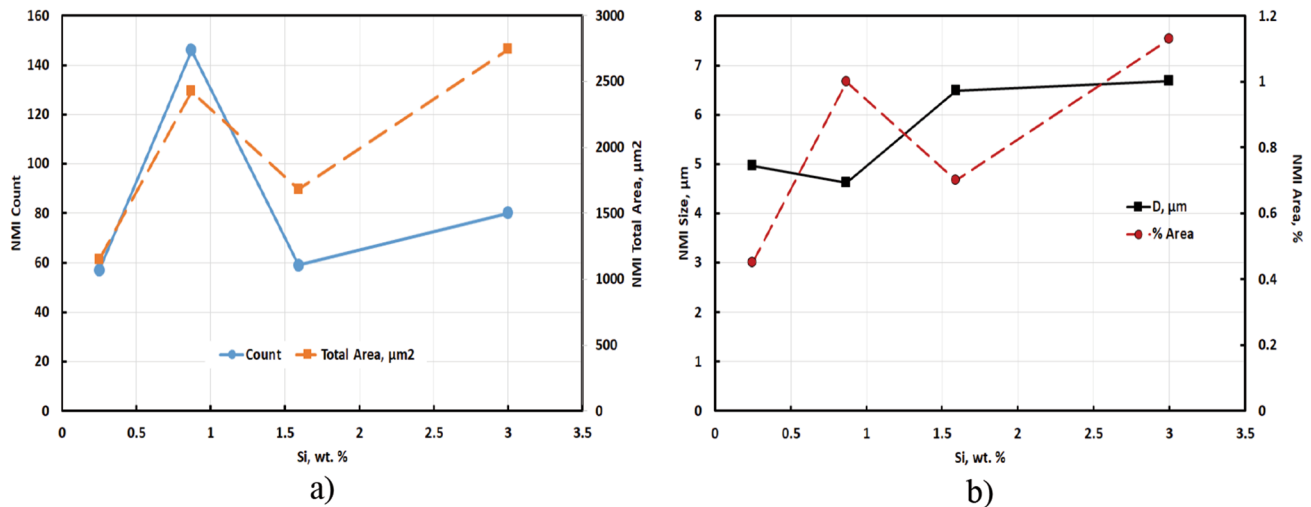


Fig. 4 The silicon content effect on the count, total area, % area, and the average size of NMI presented in investigated steel

for higher silicon content of more than 0.86 Si. The discussion mentioned above can explain the causes for the sudden change in the count and average size for steel containing more than 0.86 Si, as shown in Fig. 4.

During solidification, the presented non-metallic inclusions in this type of steel hinder the migration of grain boundaries, resulting in grain growth (coarsening) prevention. The grain refinement has an enhancing effect on the technological behavior of the studied steel. Count, total area, area, average (arithmetic mean) size, and NMI's circularity significantly affect the surface fracture mode. Decreasing count, total area, area volume fraction %, and the average size of NMI decrease strength and ductility. The author suggests that a small-size non-metallic inclusion significantly improves mechanical properties, discussed briefly in the subsequent sections.

Microstructure Observation

Both annealing and normalizing heat treatments utilized high temperatures to heat steel above their recrystallization (RCT), then slowly cooled to room temperature. While some roles' steps change, the fundamental purpose of both is essential to enhance tensile ductility. Tensile ductility properties were enhanced through microstructural modification.

It was well-known that annealing applies a slower cooling rate than normalizing, producing non-equilibrium microstructures. It is too difficult to recognize non-equilibrium structures such as pearlite, bainite, and martensite using Thermo-Calc software. So, JMatPro software was used to fulfill the theoretical picture of the investigated steel microstructure and simulate the actual production condition.

The authors suggested normalizing heat treatment due to the many benefits from the added performance

characteristics of this specialized heat treatment. Review the impact of this process when applied by an experienced heat treatment team, e.g., improved impact toughness and tensile ductility.

The previous benefits of normalizing heat treatment may be attributed to fine, homogenous, and well-distributed microstructures. Normalizing heat treatment includes heating at a rate of 5 °C/s from room temperature until 950 °C and holding for 600 s, then cooling freely on-air (cooling at 0.5 °C/s). Figure 6 shows the expected normalized microstructure was a mixture of ferrite matrix, indeed, pearlite. Figure 6 exhibits the JMatPro results of normalizing structure and homogenizing temperature. Otherwise, Fig. 7 displays the optical microstructure of investigated steels. Table 8 tabulates the amount of each phase presented in an investigated steel.

Table 8 includes both amounts in volume percent of microstructures expected from JMatPro software and actual normalized specimens from investigated steel using image J software analysis. Table 8 shows that the obtained structure includes pearlite plus ferrite with a précised amount depending mainly on the chemical composition of the steel melted. Also, silicon addition promotes pearlite-like carbide precipitation, in other words, increasing the percentage of pearlite with the increasing silicon content, as shown in Table 8. Therefore, for high silicon wt.%, the trend was reversed and tended to precipitate more ferrite. Therefore, this may be due to silicon being a ferrite stabilizer element, and high silicon content spreads the BCC-ferrite region and simultaneously delays pearlitic transformation.

Obtained data show that silicon additive to such steel increases the tendency to precipitate more carbide-like cementite (pearlite). Microstructure photos of normalized steel specimens emphasize that the austenite phase is too

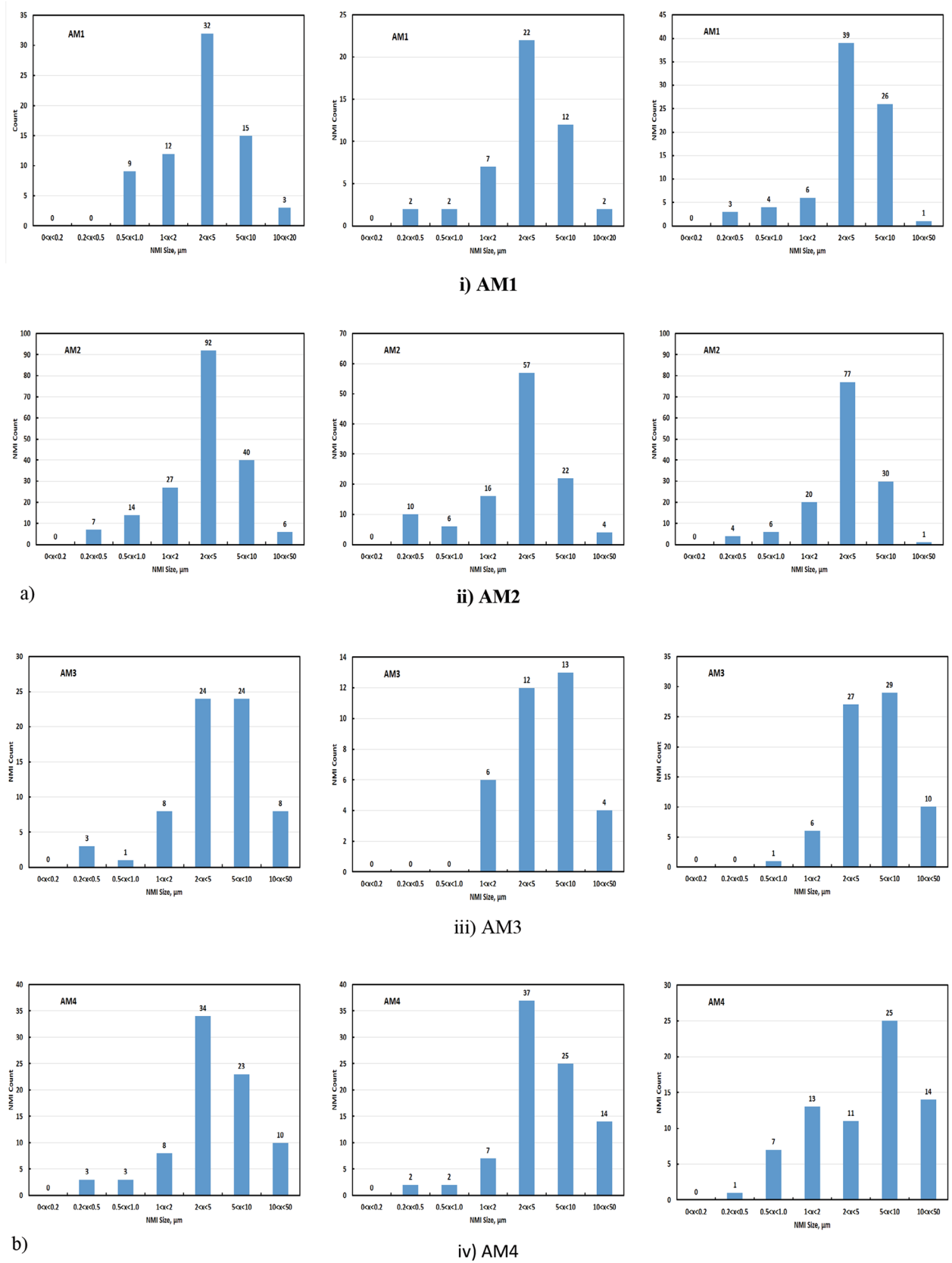


Fig. 5 a Distribution of non-metallic inclusions of studied steel. b Distribution of non-metallic inclusions of studied steel

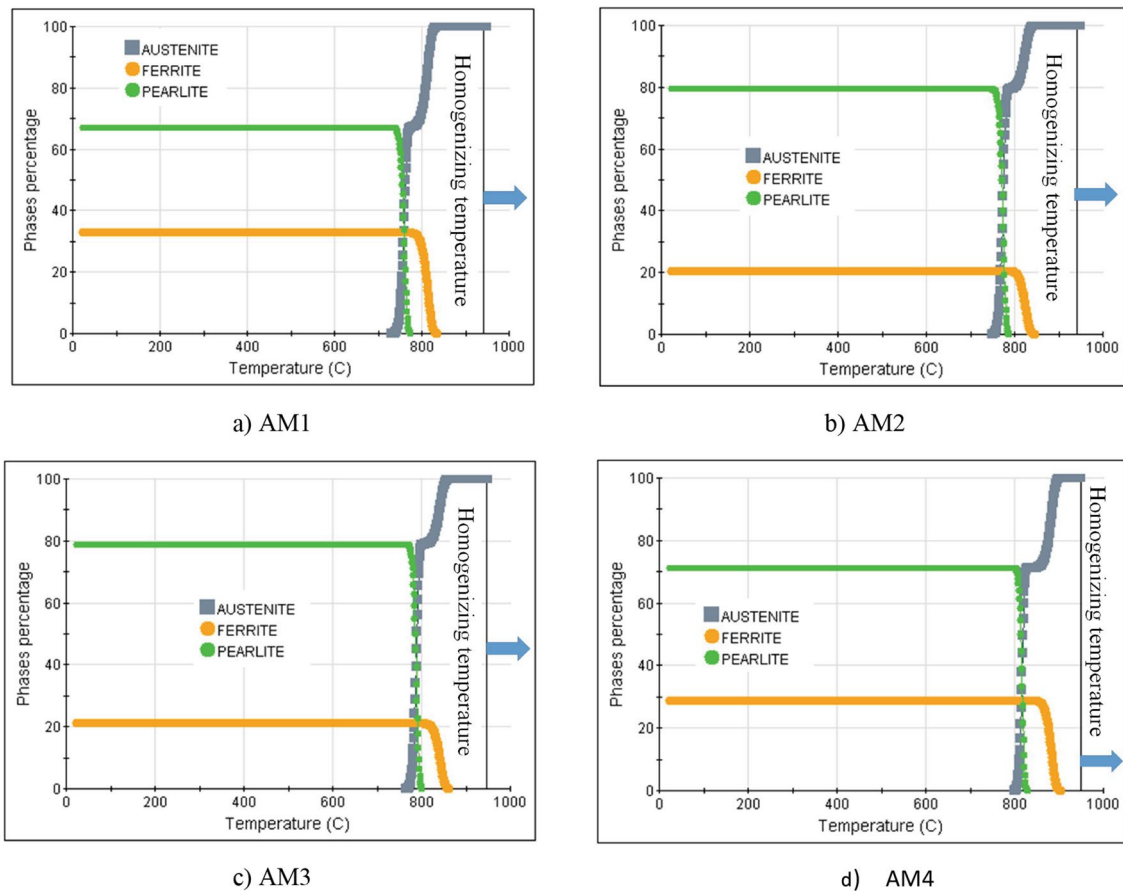


Fig. 6 JMatPro results of normalizing structure and homogenizing temperature

hard to recognize due to its minute percentage; consequently, the obtained microstructure mainly consists of ferrite–pearlite, as shown in Fig. 7.

Figure 7 shows the microstructure of investigated steel that indicated a mixed microstructure dominated by ferrite-looking white, in addition to the second phase of pearlite morphology. The amount and size of different phases obtained vary with the silicon content. An increase in investigated steel’s silicon content dominates the grain size decrease. Pearlite phase-volume % increases by increasing the silicon content up to 1.59 Si%. On the contrary, at a high silicon content of 3%, pearlite volume % decreases due to high ferritic-stabilizing element content, leading to an increase in the tendency of BCC-phase (ferrite) formation and a diminishes in the amount of the pearlite in the finished microstructure. The austenite phase starts on the pearlite phase, so the amount and size of pearlite is a significant parameter in consequent production steps.

Determination of Transformation Temperature

The metallurgist knows that transformation and homogenization temperatures are affected by initial chemical composition, grain size, initial microstructure, and heating rate. Changes in silicon contents significantly affect transformation temperatures A_{c1} and A_{c3} .

To ensure the transformation temperature of investigated steels, the authors use a practical published equation, JMatPro software, and a dilatometer test experimentally.

Practical Published Equation

Lower and upper austenitizing temperatures (limits of the austempering process), therefore, the start temperature of bainite (B_s) and martensite (M_s), were determined theoretically employing applicable published data [48–51]. Table 9 shows the chemical composition valid for the employed J. TRZASKA [51] equation, which invented the critical temperatures formula for selected silicon-containing steel. Equation (3) to (6) were utilized to calculate the critical transformation temperature

Fig. 7 Microstructure of investigated normalized steels

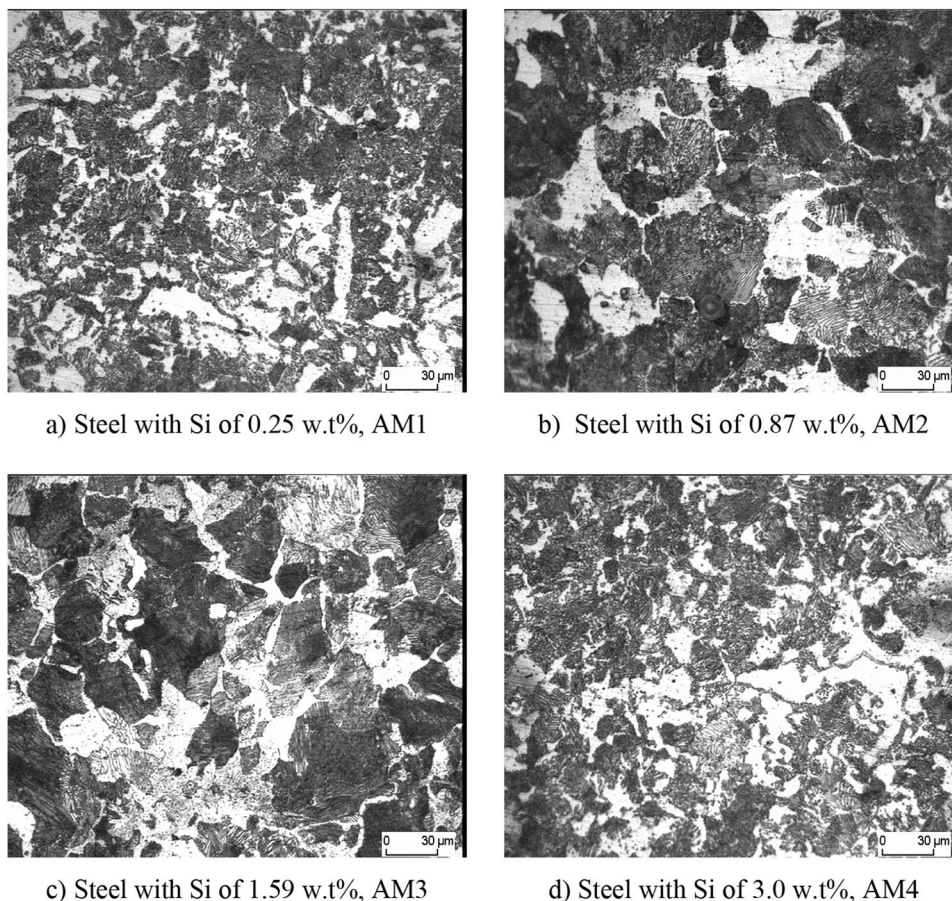


Table 8 The amount of different phases presented and the homogenization temperature of an investigated steel

Steel no.	Microstructure, %				Homogenization temperature > T, °C	
	Jmat		Image analysis		Dilatometer (AC3 + 100)	JMatPro
	Ferrite	Pearlite	Ferrite	Pearlite		
AM1	26	74	44	56	925	940
AM2	20	80	32	68	930	942
AM3	22	78	37	63	962	947
AM4	29	71	39	61	982	950

Table 9 Chemical composition valid for used practical J. TRZASKA equation [47]

Mass fraction of elements, %							
C	Mn	Si	Cr	Ni	Mo	V	Cu
0.06–0.68	0.13–2.04	0.12–1.75	0–2.3	0–3.85	0–1.05	0–0.38	0–0.38

Ac1 and Ac3 beside the bainitic and martensitic start temperature of investigated steel. Table 9 tabulates the validated chemical composition of the J. TRZASKA [51].

$$Ac1 = 742 + 36Cu + 45V - 16Mo - 17Ni - 16Cr - 14Mn + 13Si - 29C \tag{3}$$

$$Ac3 = 925 + 97V + 13Mo - 16Ni - 7Mn + 39Si - 219\sqrt{C} \tag{4}$$

$$Ms = 541 - 17Mo - 18Ni - 14Cr - 36Mn - 10.5Si - 401C \tag{5}$$

$$Bs = 771 - 41V - 55Mo - 31Ni - 58.5Cr - 69Mn - 23Si - 231.5C \tag{6}$$

According to J. TRZASKA [47] Equation (4), the Ac3 (°C) average upper critical transformation temperature (austenitizing) of the tested chemical composition is estimated to be more than 900 °C. Thus, a more than 950 °C temperature was chosen to become an austenitized temperature in the present study.

JMatPro Software

JMatPro software is valuable for theoretically calculating the investigated steel’s critical temperature. The data obtained by JMatPro software are close to data obtained using the J. TRZASKA [51] formula, and the difference between the two methods is in the range of $\pm 2\%$. The critical temperatures for steel number AM4 have a higher difference because its silicon content is out of the range referred to in the J. TRZASKA formula.

Figure 8 collects the CCT diagrams of the investigated steel. This figure stresses that silicon moves the transformation starting temperature of ferrite into austenite at a higher

temperature. Also, Fig. 8 shows a decrease in bainitic and martensitic transformation starting temperatures. Silicon addition increases the flattening of bainitic starting temperature, producing homogeneous microstructure from surface to core. Critical transformation temperatures are collected in Table 10.

Table 10 shows a deviation of up to $\pm 8\%$ between the critical transformation temperature of investigated steel calculated by J. TRAZASKA equation and data measured experimentally using dilation. This deviation reached $\pm 11\%$ using the JmatPro program compared to dilation data. The deviation in the obtained result may be attributed to the difference in chemical composition, or the effect of environment rate may not be considered during the model (equation of J. TRAZASKA or JmatPro).

Dilatometry Test

Dilatation tests were done to get the actual transformation temperatures of investigated steels under the same conditions used in the simulation by JMatPro. The dilatation test

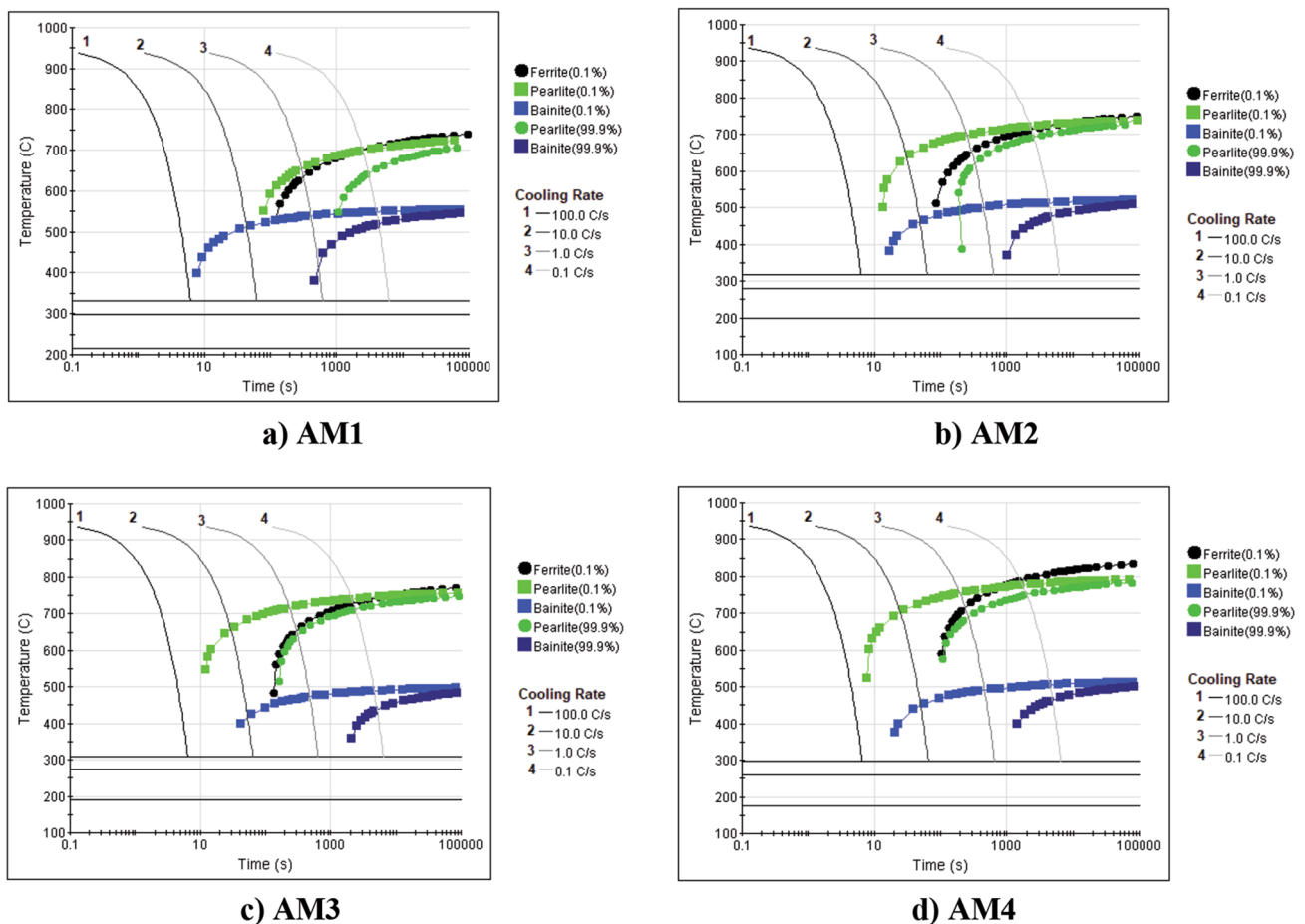


Fig. 8 CCT diagram of investigated steel

Table 10 Theoretically calculated critical temperatures using an experimental formula, JMatPro software, and experimentally measured using a dilatometer test accompanied with calculated error rate (a) Ac1 (b) Ac3 (c) martensite start, Ms (d) bainitic start, Bs

Sample No.	Heat treatment parameters, Temp. °C				
	Theoretical		Experimental Dilation	Calculated errors rate	
	Calculated, equation	JmatPro		Calculated, equation	JmatPro
(a)					
	Ac1	Ac1	Ac1	Ac1	Ac1
AM1	728	739	707	2.97	4.53
AM2	735	748	718	2.37	4.18
AM3	746	765.5	749	− 0.40	2.20
AM4	765	800	772	− 0.90	3.63
(b)					
	Ac3	Ac3	Ac3	Ac3	Ac3
AM1	785	761	809	− 2.97	− 5.93
AM2	805	772	830	− 3.01	− 6.99
AM3	836	794	862	− 3.02	− 7.89
AM4	895	858	882	1.47	− 2.72
(c)					
	Ms	Ms	Ms	Ms	Ms
AM1	334	332	345	− 3.19	− 3.77
AM2	319.3	317	343	− 6.91	− 7.58
AM3	316.5	310	342	− 7.46	− 9.36
AM4	312	297	335	− 6.87	− 11.34
(d)					
	Bs	Bs	Bs	Bs	Bs
AM1	548	557	505	8.51	10.30
AM2	535	524	495	8.08	5.86
AM3	514.8	501	494	4.21	1.42
AM4	488	516	468	4.27	10.26

is done at a heating rate equal to 5 °C/s from room temperature until the austenitization temperature, e.g., Ac3 + 100 °C and holding for 600 s, then cooling 0.5 °C/s until room temperature is reached. Figure 9 shows the dilatation curves of investigated steel and its 1st derivative for the heating and cooling parts, respectively.

Dilatometer results show that the critical temperatures of investigated steel are too close to the data obtained theoretically by the empirical equation invented by J. TRZASKA [51] and by simulation done through the JMatPro program. The first derivative with the time of dilatation curve reported that non-recrystallization temperature (T_{nr}) significantly increases with increasing silicon contents, as shown in Fig. 9 and Table 9. According to the data obtained from ThermoCalc and JMatPro software, in addition to the dilatometer test, the authors decided on the methodology and material

balance calculations for producing such steel for verifying the designed technological properties.

Figure 10 shows the schematic diagram of the forging process depending on data extracted from Thermo-Calc, JmatPro, and the dilatometry test. This figure shows the forging conditions needed for the manufacturing process of such steels. The forged operation was done according to the data extracted from the data obtained by JMatPro software and the dilatation test. Figure 11 shows the microstructure observation of the studied steel after the forging operation.

Heat Treatment

Implementing the plan to achieve this work's essential objective, which is to manufacture economical high-strength steel with moderate stress of nearly 1100 MPa with total engineering strain > 10%, the previous sections show that mechanical properties cannot be determined only by chemical composition—designed mechanical properties verified through control of the microstructure of the final product.

The microstructures of the final product are controlled through the chemical composition of the investigated steel specimens, the production technology, refining, and cleanliness methodology. Also, thermomechanical forming and heat treatment remarkably affect the final microstructure. Furthermore, the well-designed heat treatment cycle is a milestone step in producing such steel and attaining the designed mechanical properties. Designed heat treatment cycles are determined by knowing different conditions; for example, the initial phase structure, the heating rate, the holding time, the austenitization temperature, the initial austenite grain size, and the cooling rates are determined parameters. Table 11 records all mentioned parameters.

By applying the above heat treatment parameters in Table 11, which is suggested based on the mentioned results, the expected microstructure using JMatPro software is collected in Fig. 12. Table 12 illustrates the data analysis extracted from Fig. 12. Both Table 12 and Fig. 12 emphasized that by controlling the chemical composition and all conditions of heat treatment of the designed strength grade (1100 MPa and > 10% Elongation) can be obtained, but with totally different microstructures. The industrial applications of all investigated steels depended mainly on the other properties, e.g., wear resistance, corrosion properties, etc.

After completing the designed heat treatment, the microstructure consists of a mixture of different phases, as displayed in Fig. 13. However, Table 12 shows a small amount of martensite lower than 1% included in the final microstructure. Furthermore, Table 12 reveals that both bainite and ferrite structures appear to have opposite behavior with the variation in Si contents up to 3% wt., where bainite volume % decrease with the increase of

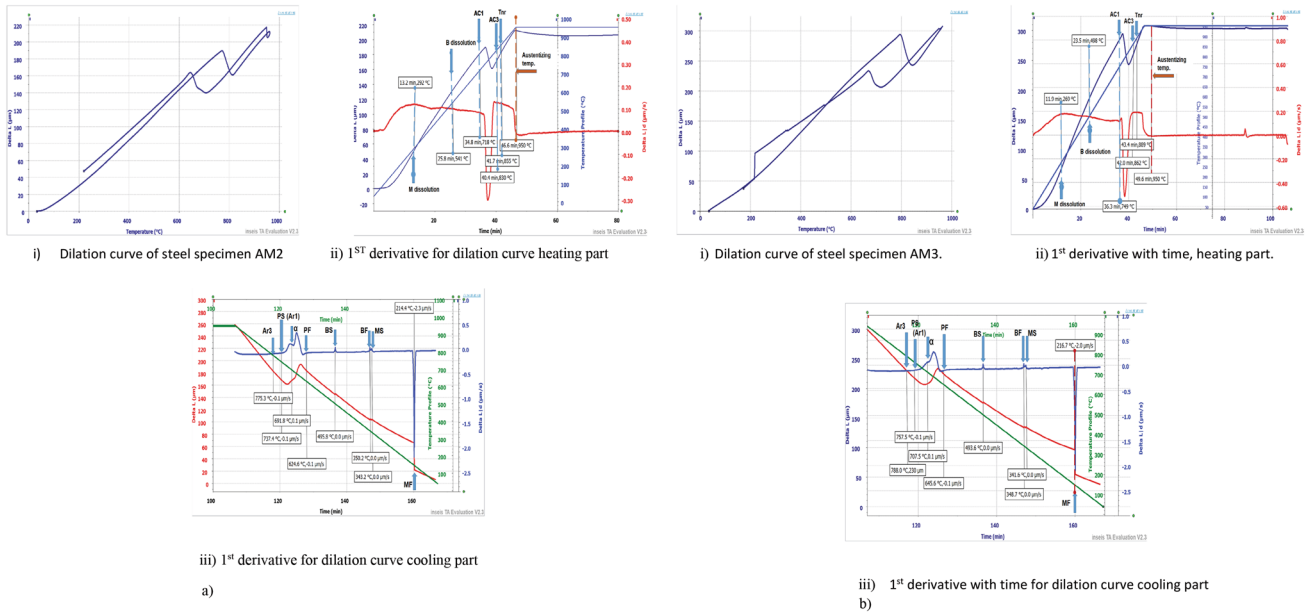
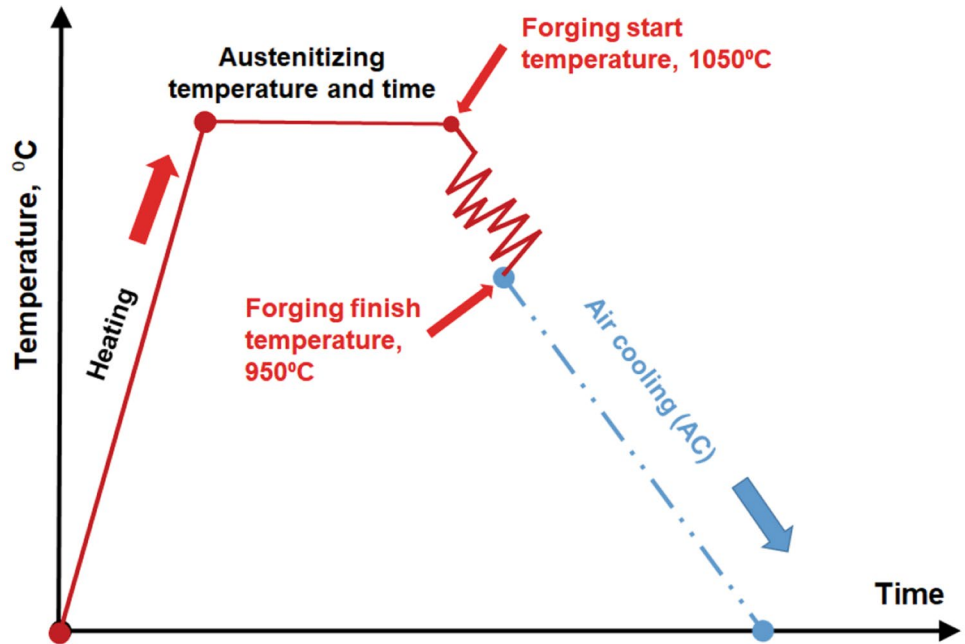


Fig. 9 a Dilation curve and its 1st derivative with the time of investigated steel, AM2. b Dilation curve and its 1st derivative with the time of investigated steel, AM3

Fig. 10 The forging cycle based on the result of JMatPro and dilatometer



silicon percentage, and on the contrary, pearlite percentage increase with raising in silicon content.

Mechanical Properties

Variations in tensile properties include engineering strain (%), ultimate engineering tensile strength (UTS), and engineering yield strength (YS), in addition to impact toughness and hardness at designed heat treatment conditions are presented in Table 13. The mechanical properties of

Fig. 11 Microstructure of investigated as-forged steels

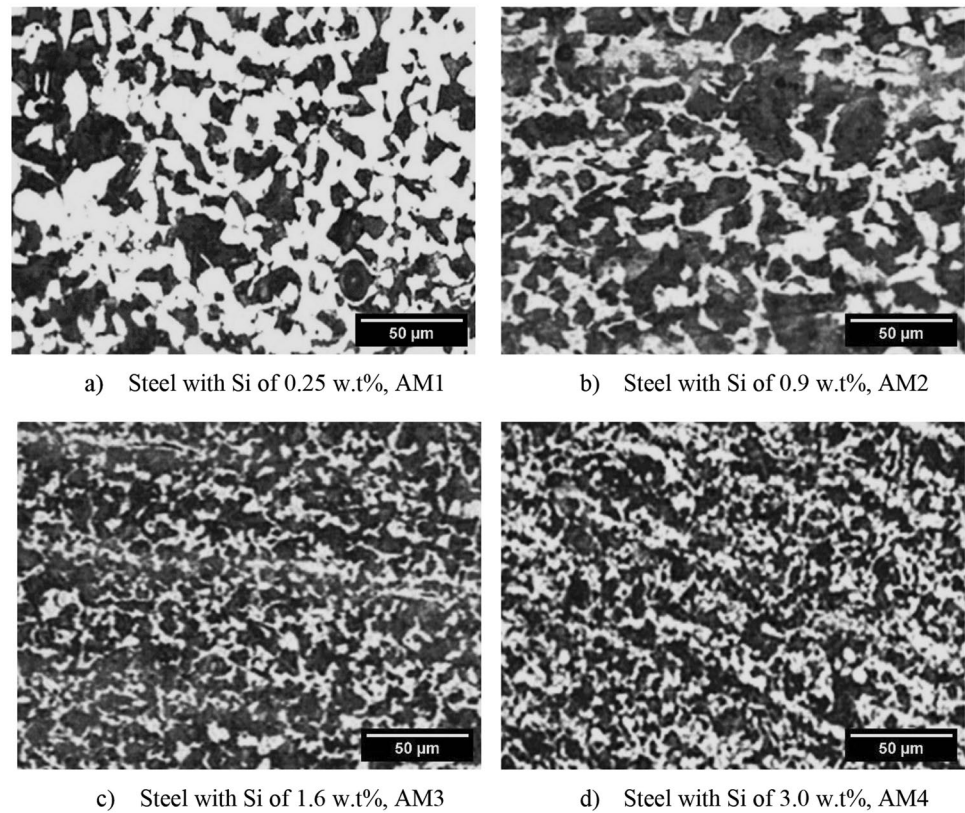


Table 11 Heat treatment parameter

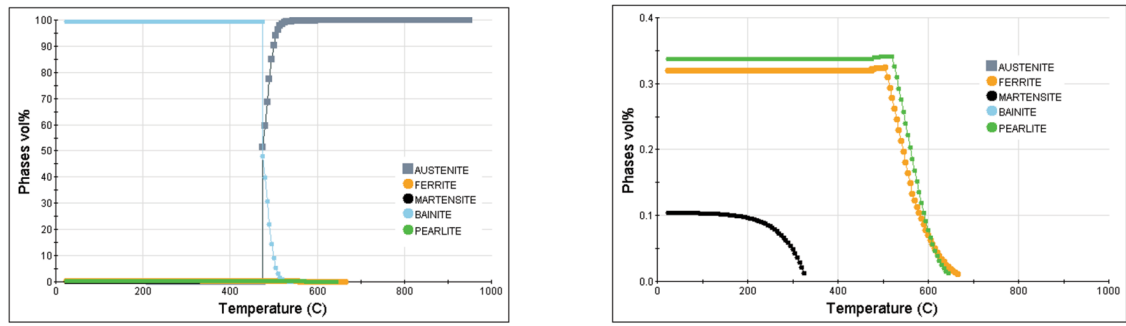
Steel no.	Heating rate, °C/s	Austenitization temperature, °C/s	Holding time, s	Austenite grain size, μm	Cooling rate, °C/s	Step temperature, °C/s	Holding time, s	Final uniform cooling rate °C/s
AM1	5	950	600	30	3	475	600	0.5
AM2	5	950	600	12	3	475	600	0.1
AM3	5	950	600	5	5	450	600	3
AM4	5	950	600	2	2	450	600	1

the examined steel were noted to be highly susceptible to silicon additives. The mentioned sections studied the influence of silicon weight percent on microstructure, phase transformation, and non-metallic inclusions. Therefore, by controlling the amount of silicon content and optimizing the heat treatment condition, the steel producer can adjust all technological properties of the investigated steel. Table 13 shows that produced steel samples have a high difference in yield strength and tensile ductility with almost ultimate tensile strength and nearly the same hardness. A consequence investigation of the tension test specimen's fracture surface facilitates recognizing the trend of the examined steel.

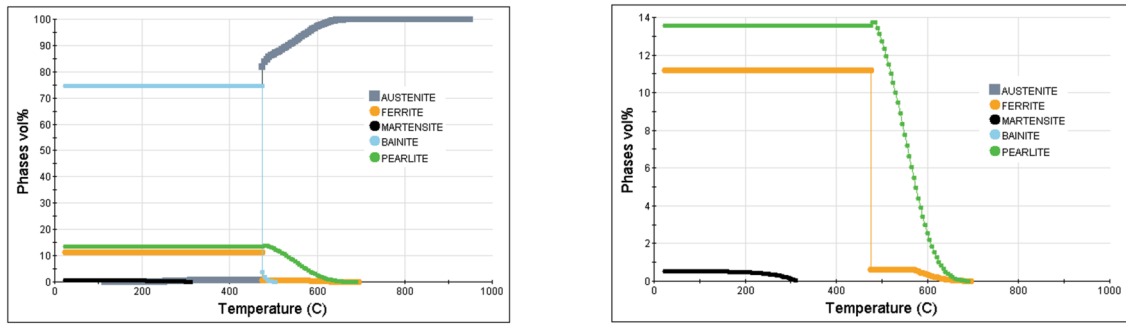
The SEM (scanning electron microscope) performed at low-magnification power was utilized to scan the broken surface of the studied steel to identify the origins of the fracture, as presented in Fig. 14. For the studied steel AM1 after

the tension test, SEM photos from the broken surface show that the predominated fracture surface is the cleavage brittle.

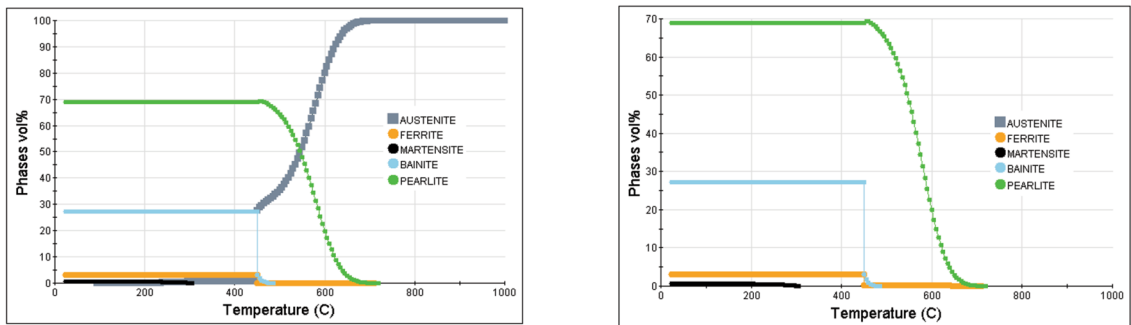
Figure 14 demonstrates the broken tensile specimen morphology of the steel alloy. The AM2 steel specimen handled through the designed heat treatment cycle principally includes dimples, as revealed in Table 10. The tensile properties and toughness of studied steel specimens are enhanced due to a small volume fraction of cleavage fracture. The steel samples' microstructure and properties are reliable with the surface fracture morphology. The dimple size would affect many factors, for example, temperature, material plasticity, the shape of the second-phase particles (NMI), deformation hardening index, and stress [52]. At a low strain rate load, uniform dimples at the beginning of the tensile test started to form inside the studied steel specimen. Denser and smaller sizes of dimples slowly agglomerated to a strip



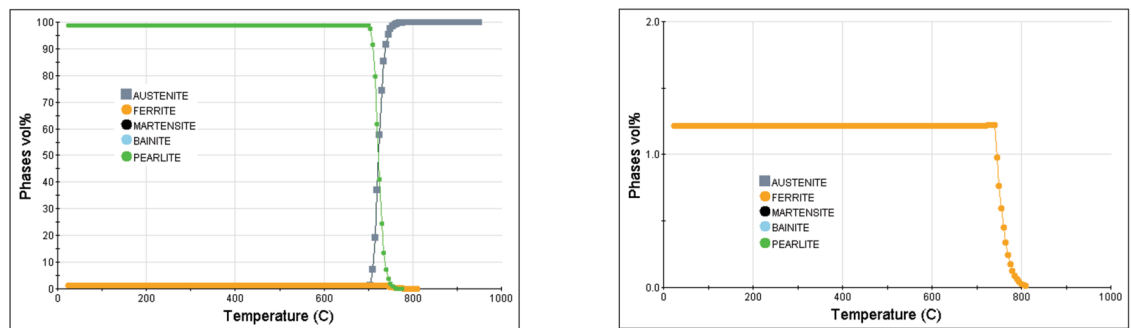
a) AM1



b) AM2



c) AM3



d) AM4

Fig. 12 Phases volume percent of heat-treated investigated steels utilizing JMatPro

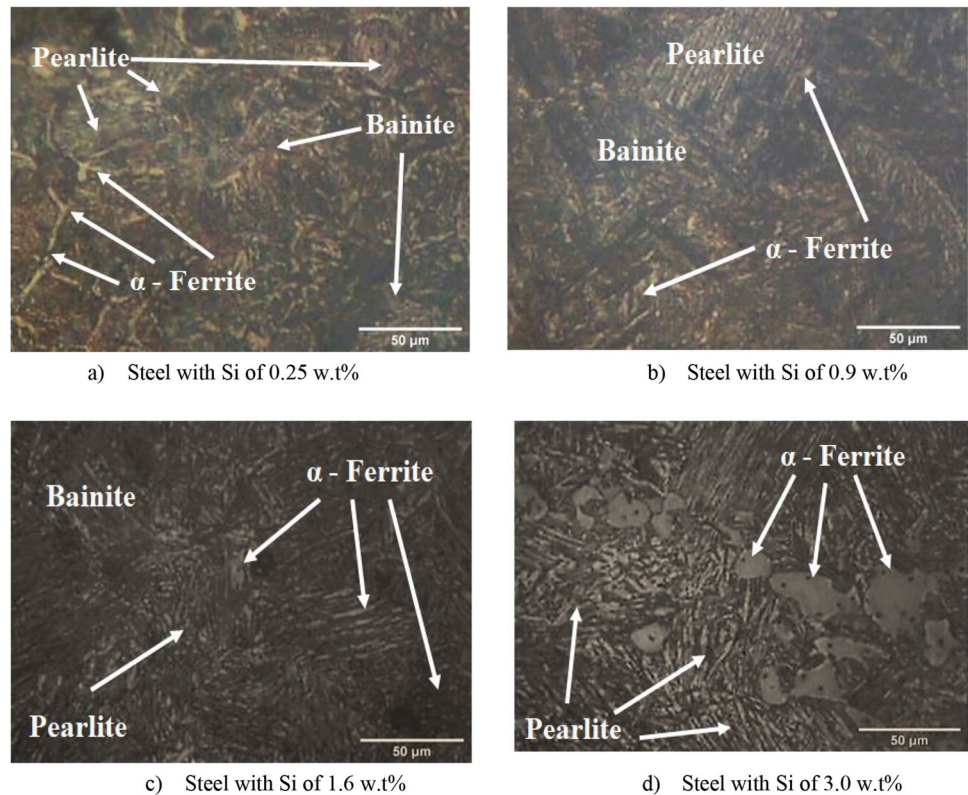
Table 12 Phases volume percent of heat-treated investigated steels utilizing JMatPro

Steel No.	Phases volume, %			
	Bainite	Ferrite	Pearlite	Martensite
AM1	99.24	0.32	0.34	0.1
AM2	74.74	11.18	13.56	0.46
AM3	27.45	2.93	69.00	0.62
AM4	0	1.21	98.79	0

when the tensile stress value reached ultimately. Some dimples had broken, and small dimples disappeared when the tensile strength value grew beyond the ultimate. The fracture source is formed easily by broken dimples, which reduce the specimens' tensile and fracture properties.

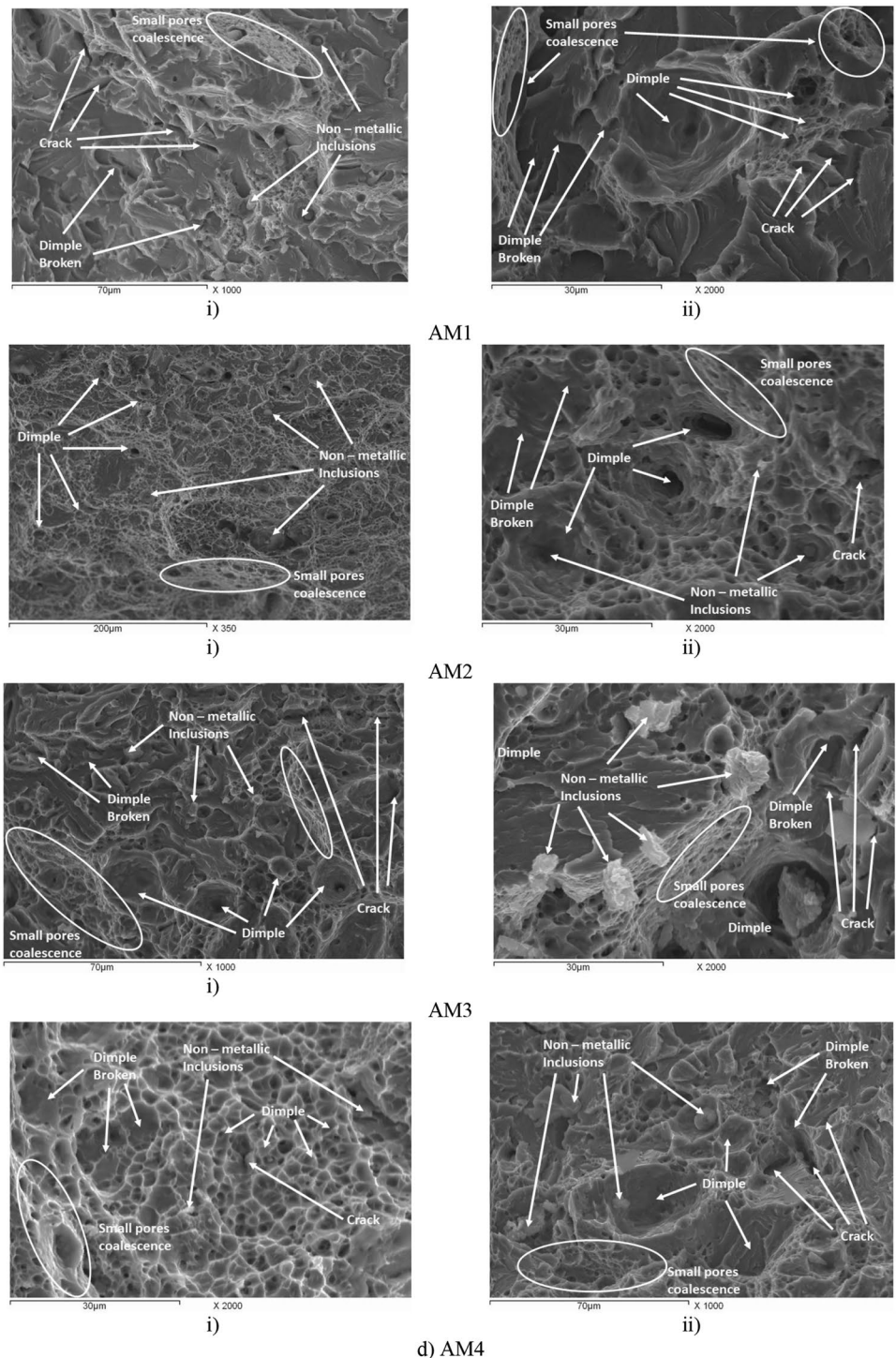
Cleavage fracture and a small number of dimples characterized the broken surface morphology of the steel AM3 specimen. Notably, the existence of dimples is considered an indicator of the elasticity or plasticity behavior during the tensile test of the steel material. The steel AM1 sample exhibits a lower ductility percent (elongation) than the AM3 steel sample, which may be attributed to the lower number of dimples, as shown in Fig. 14c.

Table 12 collects the data that emphasized this result. Furthermore, Table 12 shows the Thermo-Calc simulation calculation of the phase-volume % for investigated steel. In addition, the volume percent of carbides decreases with the increasing silicon content, as shown in Table 12. A decrease in the NMI count with a higher circulating factor was represented by utilizing image analysis. So, increasing the circulating factor enlarges the matching between NMI and its

Fig. 13 Microstructure of investigated austempered steels**Table 13** Mechanical properties of experimental steels

Steel sample no.	Hardness		Tensile properties			Impact toughness (J)
	HB	HRC	YTS, MPa	UTS, MPa	Elongation, ϵ_T %	
1	262	27	660	906	10.8	45
2	300	32	853	1113	16.2	56
3	331	36	852	1121	12.1	52
4	331	36	746	1001	8.6	48

Fig. 14 The fracture surface morphology of the studied tensile steel specimens



circumstances and decreases the chances of crack formation and initiation.

Following the range of tested chemical composition and production conditions, all investigated steel samples have lower non-metallic inclusions (carbide, nitride, oxides, etc.) and content with a small size, which stops the crack from propagation. A simultaneous increase of elongation percent

and strength value (tensile properties) may be attributed to small-sized NMI. Table 12 records the Charpy impact toughness energy and tensile properties results.

Fig. 15 displays a scanning electron microscope at higher magnification. In addition, Fig. 15 emphasizes the existence of NMI (non-metallic inclusion) with an extensive area $> 2 \mu\text{m}^2$ in the case of the AM3 steel sample. The prior NMI

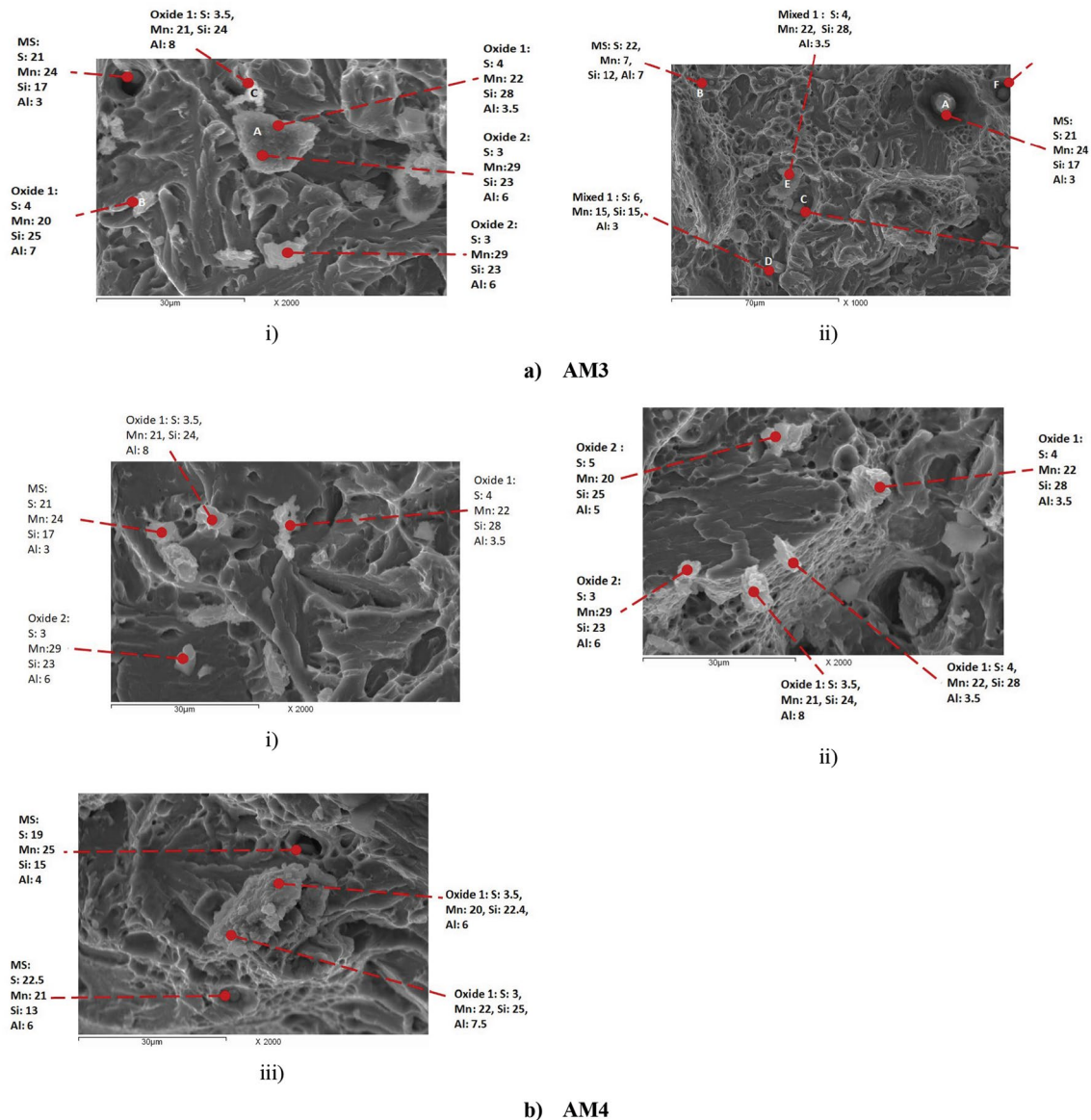


Fig. 15 Non-metallic inclusions in tensile fracture surface of investigated steel

worked as a crack initiation and formation site. Figure 15 reveals that non-metallic inclusions are predominantly silicon-manganese oxides, and silicon oxides increase with the silicon contents in the studied steel. Furthermore, Fig. 15 demonstrates that the circularity of the present non-metallic inclusions decreases to a large extent. Figure 15 illustrates the non-metallic inclusion in sulfide form is also present in the broken surface.

The large NMI (non-metallic inclusions) influences diminish all the mechanical properties of examined steel, e.g., the AM4 steel sample. Furthermore, Fig. 15c illustrates the large-size non-metallic inclusions attending in steel AM4. The mentioned non-metallic inclusion has a size of $> 25 \mu\text{m}$ with a circulatory factor lower than 0.5.

Therefore, this type of inclusion was considered the location of initiation and formation of cracks, in addition to stress concentration, that deteriorate all tensile ductility properties and impact energy toughness, as revealed in Table 12.

In the case of steels, the AM4 sample contained higher silicon content of about 3 wt.% silicon broken surfaces designated quasi-cleavage fracture mode, considered a mixed fracture mode. Corresponded with the AM1 steel specimen that indicates the cleavage fracture, the quasi-cleavage fracture with a river pattern in the AM4 steel sample after the third condition of heat treatment (Fig. 15c) is a part of ductile fracture that demonstrates the growth of strain, %. On the other hand, the amount (depth and size) of dimples in

the AM4 steel sample is more significant than in the AM1 steel specimen.

It can be concluded that the silicon content of the steel samples reached 3%, and the tensile properties and toughness deteriorated compared with AM1, which contains 0.25% Si. The previous result may be due to the steel AM4 sample containing a large percentage of cleavage fracture. The microstructure and properties of the steel samples are consistent with the fracture morphology.

Conclusions

1. The silicon additive has a remarkable influence on thermodynamical equilibria properties of investigating steels, in addition to having a notable impact on the volume fraction and precipitated constituent's chemical composition.

2. The silicon additive (> 0.25 wt.%) promotes M_7C_3 carbide formation instead of $M_{23}C_7$ carbides.

3. Excess addition of silicon (> 0.25 wt.%) deteriorated the tensile ductility and increased hardness. Furthermore, low silicon steel content encourages quasi-ductile fracture surfaces instead of the cleavage of brittle fracture surfaces in high silicon additives.

4. High silicon additives encourage precipitate non-metallic inclusion with lower manganese and high silicon contents. High silicon additive influences NMI's count, volume fraction, circularity, and size distribution.

5. Adding 0.87–1.6 wt.% silicon resulted in the economical production of steel with an ultimate tensile strength of about 1100MPa with a total engineering strain $\geq 12\%$.

Acknowledgment The authors are gratified to the administration of the Central Metallurgical Research and Development Institute, CMRDI, Helwan-Cairo-Egypt, to support the production of research materials for this investigation. Furthermore, the authors appreciate all colleagues of the "Steel Technology Department, CMRDI" for their distinguished help and guidance in carrying out all experimental procedures. Special thanks were to Prof. Dr. Khaled Ibrahim, "Head of the Casting Department at CMRDI," for his valuable discussion and supporting article publishing.

Funding Open access funding provided by The Science, Technology & Innovation Funding Authority (STDF) in cooperation with The Egyptian Knowledge Bank (EKB).

Declarations

Conflict of interest The authors declare no conflict of interest.

Open Access This article is licensed under a Creative Commons Attribution 4.0 International License, which permits use, sharing, adaptation, distribution and reproduction in any medium or format, as long as you give appropriate credit to the original author(s) and the source, provide a link to the Creative Commons licence, and indicate if changes were made. The images or other third party material in this article are included in the article's Creative Commons licence, unless indicated otherwise in a credit line to the material. If material is not included in

the article's Creative Commons licence and your intended use is not permitted by statutory regulation or exceeds the permitted use, you will need to obtain permission directly from the copyright holder. To view a copy of this licence, visit <http://creativecommons.org/licenses/by/4.0/>.

References

1. M. Franceschi, L. Pezzato, C. Gennari et al., Effect of inter-critical annealing and austempering on the microstructure and mechanical properties of a high silicon manganese steel. *Metals*. **10**(11), 1448 (2020). <https://doi.org/10.3390/met10111448>
2. R.E. Reed Hill, *Physical Metallurgy Principles*, 2nd edn (D. Van Nostrand Company, New York, 1973)
3. D.A. Porter, K.E. Easterling, *Phase Transformations in Metals and Alloys*, 2nd edn (Chapman and Hall, 1992)
4. P.G. Shewmon, *Phase Transformations in Metals* (McGraw Hill, 1986)
5. U. Olofsson, Y. Zhu, S. Abbasi et al., Tribology of the wheel-rail contact—aspects of wear, particle emission, and adhesion. *Veh. Syst. Dyn.* **51**, 1091–1120 (2013). <https://doi.org/10.1080/00423114.2013.800215>
6. M. Masoumi, E.A.A. Echeverri, A. Tschiptschin et al., Improvement of wear resistance in pearlitic rail steel via quenching and partitioning processing. *Sci. Rep.* **9**, 7454 (2019). <https://doi.org/10.1038/s41598-019-43623-7>
7. V. Efremenko, K. Shimizu, V. Zurnadgy et al., Mechanical properties of carbide-free lower bainite in complex alloyed constructional steel: effect of bainitizing treatment parameters. *Kovove Mater.* **58**, 129–140 (2020). https://doi.org/10.4149/km_2020_2_129
8. V.T. Duong, Y.Y. Song, K.S. Park et al., Austenite in transformation-induced plasticity steel subjected to multiple isothermal heat treatments. *Metall. Mater. Trans. A.* **45**, 4201–4209 (2014). <https://doi.org/10.1007/s11661-014-2405-z>
9. H.K.D.H. Bhadeshia, *New Bainitic Steels by Design*. The University of Cambridge (2013). www.msm.cam.ac.uk/phase-trans
10. K. Bandyopadhyay, J. Lee, J. Shim et al., Modeling and experiment on microstructure evolutions and mechanical properties in grade 600 MPa reinforcing steel rebar subjected to Temp Core process. *Mater. Sci. Eng. A.* **745**, 39–52 (2019). <https://doi.org/10.1016/j.msea.2018.12.079>
11. H. Amel-Farзад, H.R. Faridi, F. Rajabpour et al., Developing very hard nanostructured bainitic steel. *Mater. Sci. Eng. A.* **559**, 68–73 (2013). <https://doi.org/10.1016/j.msea.2012.08.020>
12. F. Liu, G. Xu, Y. Zhang et al., In situ observations of austenite grain growth in FeC-Mn-Si super bainitic steel. *Int. J. Miner. Metall. Mater.* **20**, 1060–1066 (2013). <https://doi.org/10.1007/s12613-013-0834-0>
13. H.K. Sung, S.Y. Shin, B. Hwang et al., Effects of cooling conditions on microstructure, tensile properties, and Charpy impact toughness of low carbon high-strength bainitic steels. *Metall. Mater. Trans. A.* **44**, 294–302 (2013). <https://doi.org/10.1007/s11661-012-1372-5>
14. Yu.N. Simonov, D.O. Panov, S.M. Yu, Principles of design of the chemical composition of steels for forming a structure of lower carbide-free bainite under delayed cooling. *Metal Sci. Heat Treat.* (2015). <https://doi.org/10.1007/s11041-015-9894-2>
15. D.O. Panov, Yu.N. Simonov, P.A. Leonov, Formation of structure and properties of carbide-free bainite in steel 30KhGSA. *Metal Sci. Heat Treat.* **1–2**, 71–75 (2016). <https://doi.org/10.1007/s11041-016-9966-y>
16. D. Mandal, M. Ghosh, J. Pal et al., Effect of austempering treatment on microstructure and mechanical properties of high-Si

- steel. *J. Mater. Sci.* **44**, 1069–1075 (2009). <https://doi.org/10.1007/s10853-008-3203-z>
17. S.K. Putatunda, A.V. Singar, R. Tackett et al., Development of a high strength high toughness ausferritic steel. *Mater. Sci. Eng. A.* **513–514**, 329–339 (2009). <https://doi.org/10.1016/j.msea.2009.02.013>
 18. E. Vuorinen, X. Chen, In-situ high-temperature X-ray studies on the bainitic transformation of austempered silicon alloyed steels. *Mater. Sci. Forum.* **638–642**, 3086–3092 (2010). <https://doi.org/10.4028/www.scientific.net/MSF.638-642.3086>
 19. N. Fonstein, *Advanced High Strength Sheet Steels: Physical Metallurgy, Design, Processing, and Properties* (Springer, Cham, 2015) (ISBN 9783319191652:1–396)
 20. D.V. Edmonds, R.C. Cochrane, Structure-property relationships in bainitic steels. *Metall. Mater. Trans. A.* **21**, 1527–1540 (1990). <https://doi.org/10.1007/BF02672567>
 21. L.J. Zhu, W.U. Di, X.M. Zhao, Effect of silicon content on thermodynamics of austenite decomposition in C-Si-Mn TRIP Steels. *J. Iron. Steel Res. Int.* **13**, 57–60 (2006). [https://doi.org/10.1016/S1006-706X\(06\)60062-9](https://doi.org/10.1016/S1006-706X(06)60062-9)
 22. L.J. Zhu, D. Wu, X.M. Zhao, Effect of silicon addition on recrystallization and phase transformation behavior of high-strength hot-rolled trip steel. *Acta Metall. Sin. Engl. Lett.* **21**, 163–168 (2008). [https://doi.org/10.1016/S1006-7191\(08\)60034-4](https://doi.org/10.1016/S1006-7191(08)60034-4)
 23. O. Matsumura, Y. Sakuma, Retained austenite in O.4C-Si-1.2Mn steel sheet intercritically heated and austempered. *ISIJ Int.* **32**, 4–10 (1992). <https://doi.org/10.2355/isijinternational.32.1014>
 24. V. Thapliyal, A. Kumar, D. Robertson, J. Smith, Inclusion modification in Si–Mn killed steels using titanium addition. *ISIJ Int.* **55**(1), 190–199 (2015). <https://doi.org/10.2355/isijinternational.55.190>
 25. E.T. Turkdogan, R.J. Fruehan, Fundamentals of iron and steelmaking, in *The Making, Shaping and Treating of Steel, Steelmaking and Refining Volume*, vol 11, 11th edn, ed. by R.J. Fruehan (AISE Steel Foundation, Pittsburgh, 1998), pp.125–126
 26. J.S. Park, J.H. Park, Effect of slag composition on the concentration of Al₂O₃ in the inclusions in Si-Mn-killed steel. *Metall. Mater. Trans. B.* **45**, 953–960 (2014). <https://doi.org/10.1007/s11663-013-9998-2>
 27. S. Lyu, X. Ma, Z. Huang, Z. Yao, H.G. Lee, Z. Jiang, G. Wang, J. Zou, B. Zhao, Understanding the formation and evolution of oxide inclusions in Si-deoxidized spring steel. *Metall. Mater. Trans. B.* **15**(50), 1862–1877 (2019). <https://doi.org/10.1007/s11663-019-01613-0>
 28. Y. Tomita, Effect of morphology of non-metallic inclusions on tensile properties of quenched and tempered 0.4C-Cr-Mo-Ni steel. *Mater. Charact.* **34**, 121–128 (1995). [https://doi.org/10.1016/1044-5803\(94\)00057-R](https://doi.org/10.1016/1044-5803(94)00057-R)
 29. S. Paul, A. Ray, Influence of inclusion characteristics on the formability and toughness properties of a hot-rolled deep-drawing quality steel. *J. Mater. Eng. Perform.* **6**, 27–34 (1997). <https://doi.org/10.1007/s11665-997-0028-x>
 30. H. Suito, R. Inoue, Thermodynamics on control of inclusions composition in ultraclean steels. *ISIJ Int.* **36**, 528–536 (2007). <https://doi.org/10.2355/isijinternational.36.528>
 31. L. Jiang, K. Cui, Quantitative study of modification of sulphide inclusions by calcium and its effect on the impact toughness of a resulfurised alloy steel. *Steel Res.* **68**, 163–168 (1997). <https://doi.org/10.1002/srin.199700558>
 32. F. Sun, K. Geng, F. Yu et al., Relationship of inclusions and rolling contact fatigue life for ultra-clean bearing steel. *Acta Metall. Sin.* **56**, 693–703 (2019). <https://doi.org/10.11900/0412.1961.2019.00337>
 33. M. Imagumbai, T. Takeda, Influence of calcium treatment on sulfide-and oxide-inclusions in continuous-cast slab of clean steel—dendrite structure and inclusions. *ISIJ Int.* **34**, 574–583 (1994). <https://doi.org/10.2355/isijinternational.34.574>
 34. Z. Wang, Q. Liu, F.M. Xie et al., Model for prediction of oxygen required in BOF steelmaking. *Ironmak. Steelmak.* **39**, 228–233 (2012). <https://doi.org/10.1179/1743281211Y.0000000085>
 35. F. Akhtar, Estimation of inclusion in forged steel through ultrasonic imaging technique. *Int. J. Res. Appl. Sci. Eng. Technol.* **7**, 1044–1052 (2019). <https://doi.org/10.22214/ijraset.2019.9150>
 36. Y. Murakami, S. Kodama, S. Konuma, Quantitative evaluation of effects of non-metallic inclusions on fatigue strength of high strength steels. I: basic fatigue mechanism and evaluation of correlation between the fatigue fracture stress and the size and location of non-metallic inclusions. *Int. J. Fatigue.* **11**, 291–298 (1989). [https://doi.org/10.1016/0142-1123\(89\)90054-6](https://doi.org/10.1016/0142-1123(89)90054-6)
 37. Y. Murakami, H. Usuki, Quantitative evaluation of effects of non-metallic inclusions on fatigue strength of high strength steels. II: fatigue limit evaluation based on statistics for extreme values of inclusion size. *Int. J. Fatigue.* **11**, 299–307 (1989). [https://doi.org/10.1016/0142-1123\(89\)90054-6](https://doi.org/10.1016/0142-1123(89)90054-6)
 38. L. Zhang, B.G. Thomas, X. Wang, et al., Evaluation and control of steel cleanliness-review, in *Steelmaking Conference Proceedings*, vol. 85, pp. 431–452 (2002)
 39. H. Atkinson, H. Genbao, Characterization of inclusions in clean steels: a review including the statistics of extremes methods. *Prog. Mater. Sci.* **48**, 457–520 (2003). [https://doi.org/10.1016/S0079-6425\(02\)00014-2](https://doi.org/10.1016/S0079-6425(02)00014-2)
 40. K. Uemura, M. Takahashi, S. Koyama et al., Filtration mechanism of non-metallic inclusions in steel by ceramic loop filter. *ISIJ Int.* **32**, 150–156 (1992). <https://doi.org/10.2355/isijinternational.32.150>
 41. T.A. Khalifa, Effect of inclusions on the fatigue limit of a heat-treated carbon steel. *Mater. Sci. Eng. A.* **102**(2), 175–180 (1988). [https://doi.org/10.1016/0025-5416\(88\)90572-1](https://doi.org/10.1016/0025-5416(88)90572-1)
 42. L.J. House, R. Rungta, A review of advances in noninvasive methods for detection and characterization of inclusions, in *Proceedings of a symposium held in a conjunction with the 1988 World Materials Congress on "Inclusions and their Influence on Material Behavior"*, Illinois, pp. 93–108 (1988)
 43. C. Gu, J. Lian, Y. Bao et al., Numerical study of the effect of inclusions on the residual stress distribution in high-strength martensitic steels during cooling. *Appl. Sci.* **9**, 455 (2019). <https://doi.org/10.3390/app9030455>
 44. A. Barbangelo, Influence of non-metallic inclusions on fatigue crack growth in a structural steel. *J. Mater. Sci.* **20**, 2087–2092 (1985). <https://doi.org/10.1007/BF0112291>
 45. H. Halfa, Characterization of electroslag remelted super hard high speed tool steel containing niobium. *Steel Res. Int.* **84**, 495–510 (2013). <https://doi.org/10.1002/srin.201200332>
 46. B. Sundman, B. Jansson, J.O. Andersson, The thermo-calc databank system. *Calphad.* **9**, 153–190 (1985). [https://doi.org/10.1016/0364-5916\(85\)90021-5](https://doi.org/10.1016/0364-5916(85)90021-5)
 47. G.C. Coelho, J.A. Golczewski, H.F. Fischmeister, Thermodynamic calculations for Nb-containing high-speed steels and white-cast-iron alloys. *Metall. Mater. Trans. A.* **34**, 1749–1758 (2003). <https://doi.org/10.1007/s11661-003-0141-x>
 48. C. Liu, Z. Zhao, D.O. Northwood et al., A new empirical formula for the calculation of MS temperatures in pure iron and super-low carbon alloy steels. *J. Mater. Process. Technol.* **113**, 556–562 (2001). [https://doi.org/10.1016/S0924-0136\(01\)00625-2](https://doi.org/10.1016/S0924-0136(01)00625-2)
 49. S. Kang, S. Yoon, S.J. Lee, Prediction of bainite start temperature in alloy steels with different grain sizes. *ISIJ Int.* **54**, 997–999 (2014). <https://doi.org/10.2355/isijinternational.54.997>
 50. J. Tian, G. Xu, M. Zhou et al., Refined bainite microstructure and mechanical properties of a high-strength low-carbon bainitic steel treated by austempering below and above MS. *Steel Res. Int.* **89**, 700469 (2018). <https://doi.org/10.1002/srin.201700469>

51. J. Trzaska, Calculation of critical temperatures by empirical formulae. *Arch. Metall. Mater.* **61**, 981–986 (2016). <https://doi.org/10.1515/amm-2016-0167>
52. J.M. Hampshire, E. King, J.J.C. Hoo, *Effect of the Steel Manufacturing Process on the Quality of Bearing Steels. ASTM STP987* (American Society for Testing and Materials, Philadelphia, 1988), pp.61–80

Publisher's Note Springer Nature remains neutral with regard to jurisdictional claims in published maps and institutional affiliations.